Direct-Current and Alternating-Current Analysis of the Humidity-Sensing Properties of Nickel Oxide Doped Polypyrrole Encapsulated in Mesoporous Silica SBA-15

Rui Wang,[1] Tong Zhang,[1] Yuan He,[1] Xiaotian Li,[2] Wangchang Geng,[2] Jinchun Tu,[2] Qing Yuan[2]

[1]*State Key Laboratory on Integrated Optoelectronics, College of Electronic Science and Engineering, Jilin University, Changchun 130012, China*
[2]*College of Material Science and Engineering, Jilin University, Changchun 130012, China*

Received 16 February 2009; accepted 31 August 2009
DOI 10.1002/app.31408
Published online 13 November 2009 in Wiley InterScience (www.interscience.wiley.com).

ABSTRACT: Nickel oxide (NiO) doped polypyrrole (PPy) was encapsulated in mesoporous SBA-15. All of the synthesized samples were characterized by infrared spectroscopy, X-ray diffraction, and scanning electron microscopy. They were investigated as humidity-sensor materials at room temperature. The sensor showed excellent humidity sensitivity in the relative humidity range 11–95%. The humidity-sensing properties were very much improved by encapsulation of the NiO-doped PPy into mesoporous silica SBA-15. Finally, the sensitivity mechanism was investigated by direct-current (dc) and alternating-current (ac) analysis. The dc circuit with the instantaneous polarity reversion method was designed by us to study the dc response in different humidity environments. The conductive mechanism was established through the dc and ac investigation, and the conductive particles were identified as ions and electrons. © 2009 Wiley Periodicals, Inc. J Appl Polym Sci 115: 3474–3480, 2010

Key words: conducting polymers; electrochemistry; films; zeolites

INTRODUCTION

With the development of the society, demands for a better living environment become greater. Because humidity is a component in our environment, the measurement and control of humidity are important not only for living conditions but also for a broad spectrum of industries and technologies. The exploitation of sensing materials is one of the most important orientations in studies of sensors today. In recent years, conducting polymer/inorganic composites have attracted considerable attention for their novel physical and chemical properties and potential applications,[1–5] hence, the idea of exploring them as sensing materials.

Conducting polymers, such as polyaniline, polypyrrole (PPy) and polythiophene have been extensively studied because of their remarkable mechanical and electrical properties. Among conducting polymers, PPy has attracted considerable attention because it has a relatively good environmental stability, it is easily synthesized, and its surface charge characteristics can easily be modified during synthesis. Many reports have been published on PPy for the fabrication of humidity sensors.[6,7] We chose PPy as the organic part in the synthesis of humidity-sensing materials. Metal oxides as inorganic materials usually have good stability, and some reports have been published on the use of metal oxides to fabricate humidity sensors.[8–14] So we chose metal oxide as the inorganic part in our study. In our previous study, we found that mesoporous SBA-15 contributed to the improvement of humidity-sensing properties[15,16] because the ordered pores in SBA-15 were propitious to H_2O molecules traveling freely. When sensing materials were encapsulated in the ordered pores of SBA-15, they were protected from pollution. Although there are lots of articles about PPy/inorganic composites, no study dealing with nickel oxide (NiO) doped PPy composites encapsulated in SBA-15 has been reported so far. In this article, we doped NiO into PPy and encapsulated it in mesoporous silica SBA-15 to improve the humidity-sensing properties. Samples of SBA-15, NiO–PPy, and NiO–PPy/SBA-15 were prepared, and their sensing properties were studied. Finally, the sensing mechanism was investigated by direct-current (dc) and alternating-current (ac) analysis.

Correspondence to: T. Zhang (zhangtong@jlu.edu.cn).
Contract grant sponsor: Science and Technology Office of Jilin Province; contract grant number: 2006528.
Contract grant sponsor: Key Foundation Project of the Education Ministry of China; contract grant number: 108042.
Contract grant sponsor: National Science Fund of China; contract grant number: 60971012.
Journal of Applied Polymer Science, Vol. 115, 3474–3480 (2010)

EXPERIMENTAL

Preparation of SBA-15

The block copolymer surfactant P123 ($EO_{20}PO_{70}EO_{20}$; 2.4 g) was mixed with 75 mL of distilled water by stirring. Subsequently, 11 mL of concentrated HCl (37.5%) was added. After the mixture was stirred for 30 min, 5.1 mL of tetraethoxysilane was added dropwise under vigorous stirring at 45°C for 4 h. Then, the mixture was transferred into a stainless reactive kettle and crystallized at 100°C for 24 h. The product was filtered and washed with distilled water, and the surfactant was removed by heat treatment in air at 550°C for 8 h.

Preparation of NiO-doped PPy

Hydrated ferric chloride ($FeCl_3 \cdot 6H_2O$) was used without any purification as an oxidant for the chemical polymerization of pyrrole. Pyrrole (3.4 mL) was dissolved in 25 mL of ethanol, and the mixture was stirred for 10 min. A $FeCl_3 \cdot 6H_2O$ ethanol solution (20 mL, 0.36 mol/L) was added dropwise to the ethanol solution of pyrrole. Then, NiO powder (1.0 g) was added to the solution with strong stirring. Instantaneously, a black precipitate was observed. The mixture was magnetically stirred for 24 h at room temperature. The resulting solution was filtered and washed three times with ethanol and then dried in a vacuum box overnight.

Encapsulation of NiO-doped PPy in mesoporous silica SBA-15

The calcined SBA-15 was vacuumed to 10 Pa at 573 K for 24 h to remove air and water in the channel. Pyrrole (3.4 mL) and NiO powder (1.0 g) were added to 25 mL of ethanol under strong stirring to form a suspension. Subsequently, 1.0 g of this SBA-15 was immersed in the suspension and kept for 24 h without stirring. Then, 25 mL of the ethanol solution of $FeCl_3 \cdot 6H_2O$ was added at room temperature under magnetic stirring for 24 h. Finally, the product was washed with ethanol and dried *in vacuo*.

Methods of characterization

X-ray powder diffraction (XRD) patterns were collected on a D8 Tools XRD instrument with Cu Kα radiation at 40 kV and 30 mA. Infrared (IR) spectra were taken on a PerkinElmer series with a resolution of 4 cm^{-1}, and the samples were prepared in the form of KBr pellets with a thickness of about 1.3 mm. Each spectrum was collected at room temperature under atmospheric pressure. The morphology of the PPy products was characterized by a JEOL JSM-6700F field emission scanning electron microscope. The characteristic curves of humidity sensitivity were measured on a ZL-5 model LCR analyzer (Shanghai, China) at room temperature. The controlled humidity environments were achieved with supersaturation aqueous solutions of different salts of LiCl, $MgCl_2$, $Mg(NO_3)_2$, NaCl, KCl, and KNO_3 in a closed glass vessel at room temperature, which yielded 11, 33, 54, 75, 85, and 95% relative humidities (RHs), respectively. A ceramic substrate ($10 \times 5 \times 1$ mm^3) made of Al_2O_3 was chosen to fabricate the humidity sensors. Ag–Pd interdigital electrodes were printed on the ceramic substrate by a screen-printing technique to form a resistive humidity sensor substrate. The sample powder was ground into a paste with deionized water, then coated on the substrate, and finally baked under IR light. To make the samples surface resistant to pollution, the protective film solution was spin-coated on the surface of the humidity-sensing film.

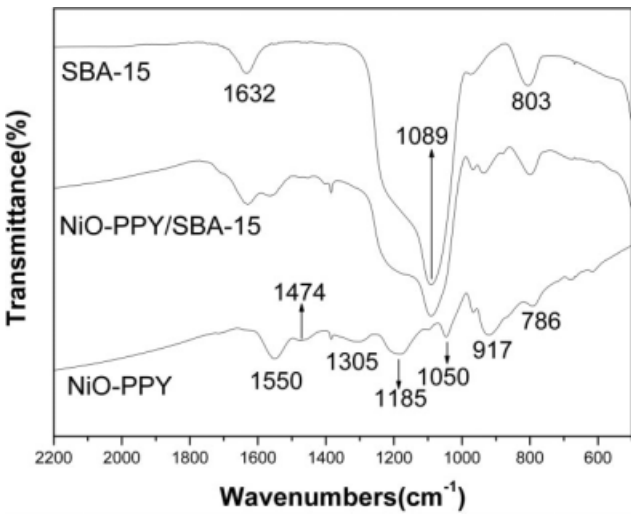

Figure 1 IR spectra of (a) SBA-15, (b) NiO–PPy/SBA-15, and (c) NiO–PPy.

RESULTS AND DISCUSSION

Structure and morphology

Figure 1 shows the IR spectra of the SBA-15, NiO–PPy/SBA-15, and NiO–PPy. As shown in Figure 1, for the mesoporous silica SBA-15, the peaks at 1089 and 803 cm^{-1} were attributed to the asymmetric stretching and symmetric modes of Si—O—Si lattice vibrations, respectively. Characteristic peaks of Si—OH were observed at 1632 cm^{-1}. All the bands were similar to results in the literature.[17,18] For NiO–PPy, the typical peaks of PPy were observed. The peak at 786 cm^{-1} was characteristic of the C—H out-of-plane bending mode. The band assigned to the C—H in-plane deformation vibration of the pyrrole rings appeared at 1050 cm^{-1}.[19] The bands observed

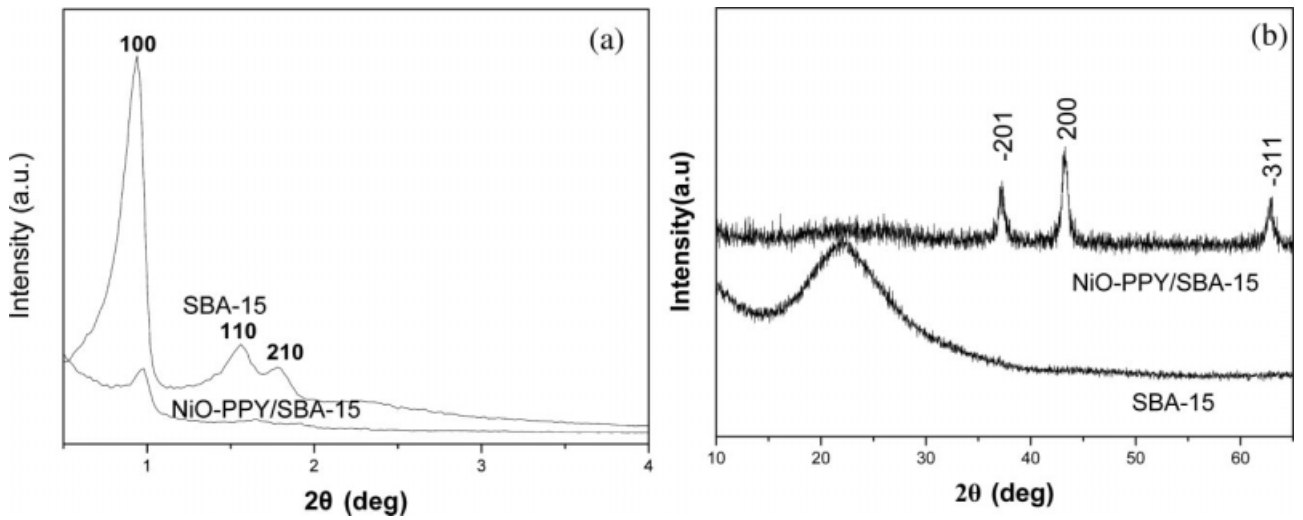

Figure 2 (a) Low-angle and (b) wide-angle XRD patterns of SBA-15 and NiO–PPy/SBA-15.

at 1474 and 1189 cm^{-1} represented the C—N stretching vibration, and this was in agreement with the literature.[20] The peak appearing at 1550 cm^{-1} came from the C=C stretching vibration. The bands at 1305 and 917 cm^{-1} were characteristic peaks of the pyrrole ring. From the IR curve, we did not observe any typical peak of NiO. After the encapsulation of NiO–PPy into the channel of mesoporous SBA-15, as shown in the curve, the peaks at 1305, 1185, and 1085 cm^{-1} belonging to PPy disappeared, and the intensity of the peaks at 1550, 1474, and 917 cm^{-1} became weaker. This phenomenon indicated the successful encapsulation of NiO–PPy into SBA-15.In addition, we did not observe any evident peaks of NiO.

The lower angle and wide-angle XRD patterns of SBA-15 and NiO–PPy/SBA-15 are shown in Figure 2. From the low-angle XRD curves [Fig. 2(a)], three peaks attributed to (100), (110), and (200) of SBA-15 were observed, which indicated the mesoporous structure of SBA-15. After the encapsulation of NiO–PPy, peaks belonging to (110) and (200) disappeared, and the intensity of (100) became weaker compared to that of SBA-15; this indicated the encapsulation of NiO–PPy into the channel of SBA-15. As shown in the wide-angle XRD curves [Fig. 2(b)], a broad peak centered at 22.2° (2θ) was observed for SBA-15. After the encapsulation of NiO–PPy into SBA-15, three peaks at 2θ values of 37.4, 43.3, and 62.8°were observed, which corresponded to ($\bar{2}$01), (200) and ($\bar{3}$11) planes of NiO and demonstrated the successful doping of NiO.

Scanning electron microscopy images of SBA-15 and NiO–PPy/SBA-15 are shown in Figure 3. For the pure SBA-15, the morphology consisted of some short rods, and this was in agreement with the literature.[15] The diameter of these rods was about 300 nm. However, when the PPy was encapsulated into SBA-15, it obtained the morphology of a bunch of rods. This morphology was similar to the morphology of pure SBA-15. These results demonstrated indirectly the successful encapsulation of NiO–PPy

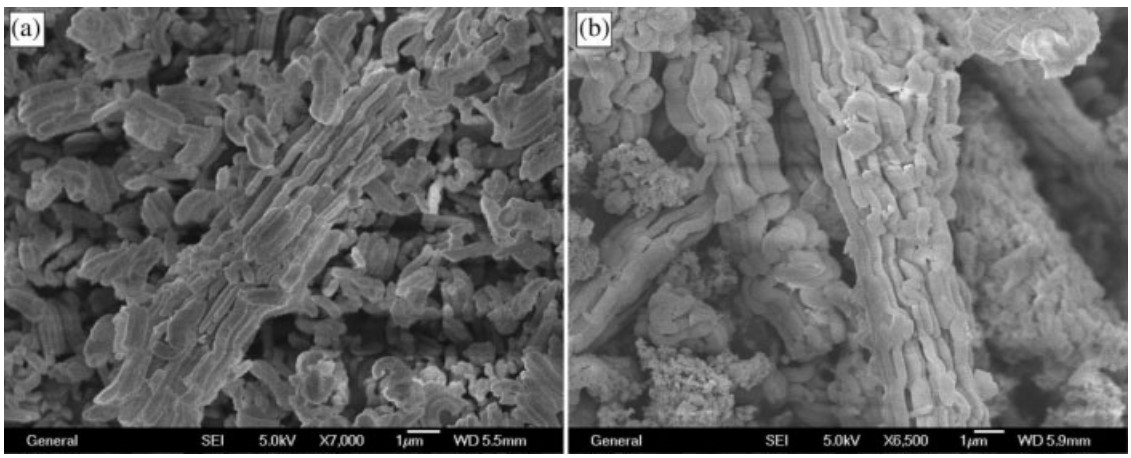

Figure 3 Scanning electron microscopy images of (a) SBA-15 and (b) NiO–PPy/SBA-15.

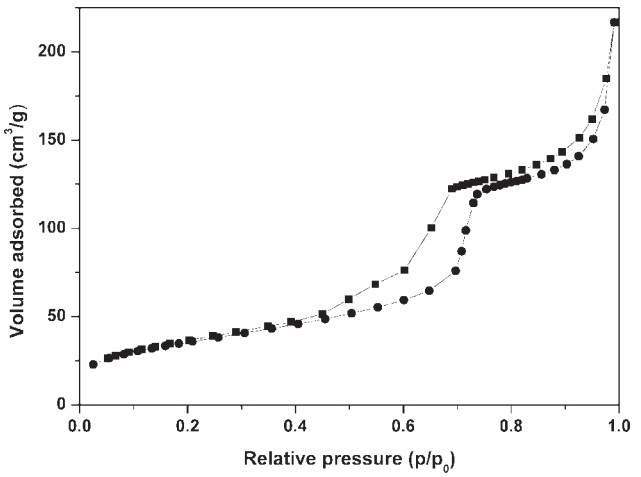

Figure 4 Nitrogen adsorption–desorption isotherms of NiO–PPy/SBA-15. p, pressure; p_o, original pressure.

into the channel of SBA-15. This was consistent with the results of IR and low-angle XRD.

To further investigate the mesoporous structure of NiO–PPy/SBA-15, the N_2 adsorption–desorption isotherm is shown in Figure 4. A type IV isotherm, which is the typical isotherm of mesoporous material, was observed. N_2 adsorption–desorption measurement exhibited that it possessed a Brunauer–Emmett–Teller surface area of 155.5 m^2/g and a total pore volume of 0.342 cm^3/g. The Brunauer–Emmett–Teller surface area and pore volume decreased greatly compared to that of pure SBA-15.[21] These results confirm the successful encapsulation of NiO/PPy into SBA-15.

Figure 5 shows the differential thermal analysis (DTA) and thermogravimetric analysis (TGA) curves of NiO–PPy/SBA-15. The TGA curve exhibited a distinct weight loss stage in the temperature range 500–600°C. The DTA curve exhibited a sharp exothermic peak at 557°C. This weight loss step from 500 to 600°C associated with the DTA peak was ascribed to the decomposition of the PPy. The peaks from 100 to 200°C referred to the removal of the residual water in the materials.

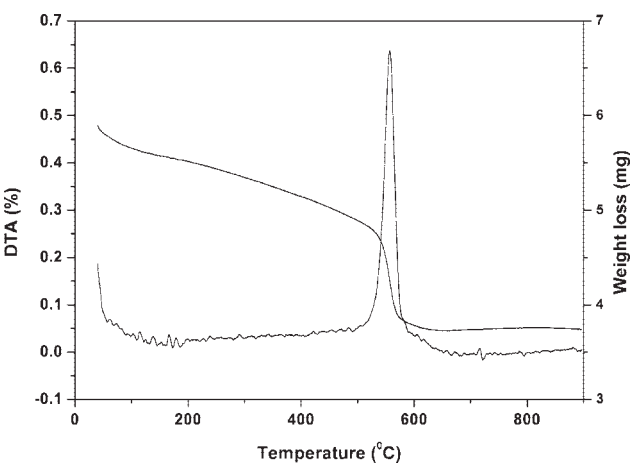

Figure 5 DTA/TGA curves of NiO–PPy/SBA-15.

Humidity-sensing properties

The impedance measurements as varied with RH at room temperature are shown in Figure 6. The measurement voltage was 1 V (ac), and the frequency was 100 Hz. For sample SBA-15, the impedance did not have any obvious decrease until the RH reached 75%. This result indicates that pure SBA-15 did not have good humidity-sensing properties. For the PPy–NiO sample, the impedance changed with RH variation, but the change was very small in the low humidity range (from 11 to 33% RH). From the curve of NiO–PPy/SBA-15, we observed that the impedance decreased rapidly with increasing RH. The humidity sensor based on NiO-doped PPy/SBA-15 had the best linearity; this indicated that NiO doping and encapsulation contributed to the improvement of the humidity-sensing properties. To evaluate the reproducibility, the impedance measured between different sensors was all in the same order of magnitude. The picture inset in Figure 6 is the impedance versus RH of the three sensors constructed in the same way and measured under the same

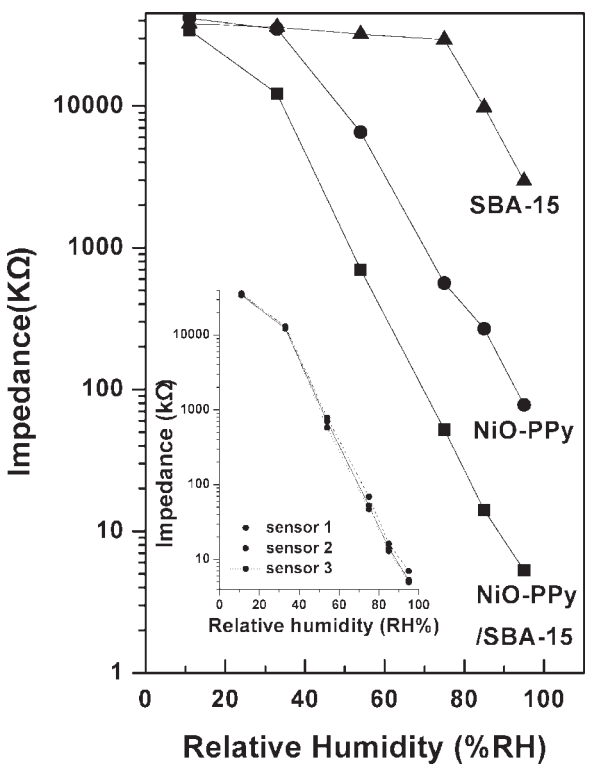

Figure 6 Humidity-sensing property curves of SBA-15, NiO–PPy, and NiO–PPy/SBA-15. The inset presents the impedance measured between different sensors.

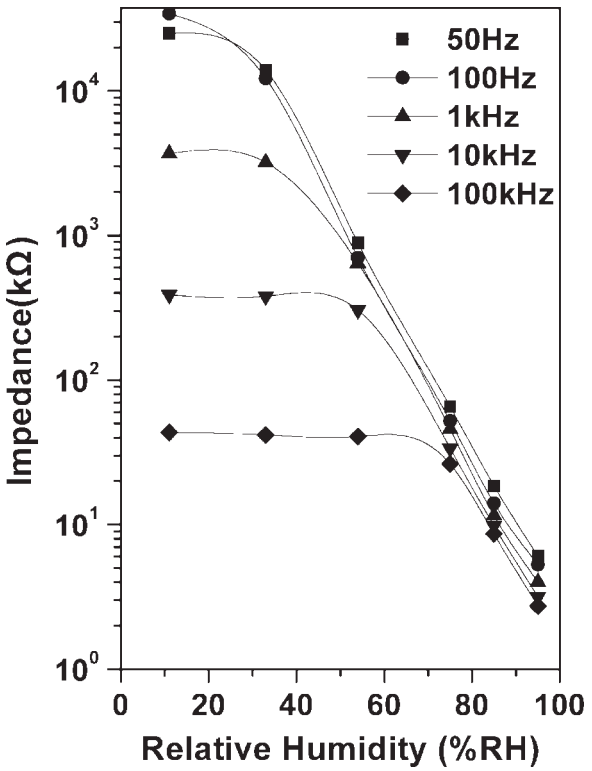

Figure 7 Relationship of the impedance and RH at different frequencies based on NiO–PPy/SBA-15.

environmental conditions. The results for different sensors constructed in the same way were satisfying.

To determine the optimal relationship of NiO–PPy/SBA-15, we measured the impedance at different frequencies, and the results are shown in Figure 7. When we chose 100 Hz as the operating frequency, the curve had the best linearity. When a lower frequency (50 Hz) was applied, the response of impedance was rather unsteady. The impedance result was lower than that when 100 Hz was applied in an 11% RH environment. After this phenomenon

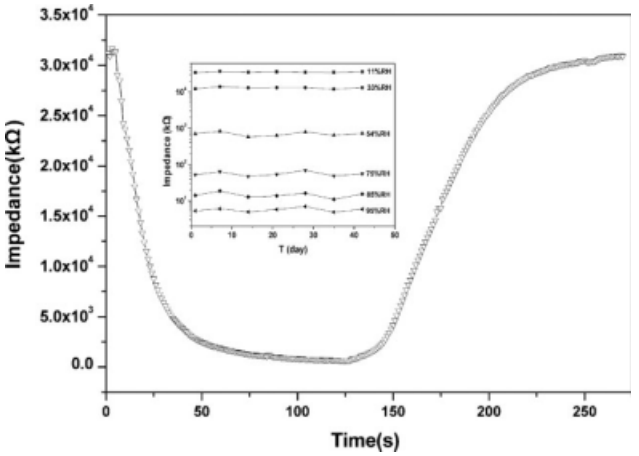

Figure 8 Response and recovery properties of the humidity sensor based on NiO–PPy/SBA-15. The inset shows the stability of the humidity sensor.

was evaluated, we chose 100 Hz as the operating frequency. It was more suitable for the humidity sensor's application. That is why we confirmed the operational conditions at 1 V (ac) and 100 Hz.

Figure 8 shows the response and recovery curve of NiO–PPy/SBA-15 corresponding to the water adsorption and desorption processes. According to the literature,[22] the time taken by a sensor to achieve 90% of the total impedance change is defined as the response time. The response time was about 45 s, and the recovery time was about 90 s as the humidity changed between 11 and 95% RH.

To evaluate the stability of the humidity sensor, we measured the humidity sensor's impedance once every week for 42 days. The supplemented data is shown in the inset in Figure 8. As shown in the curves, the impedance measured between different days was all in the same order of magnitude. The sample exhibited excellent stability, and there was

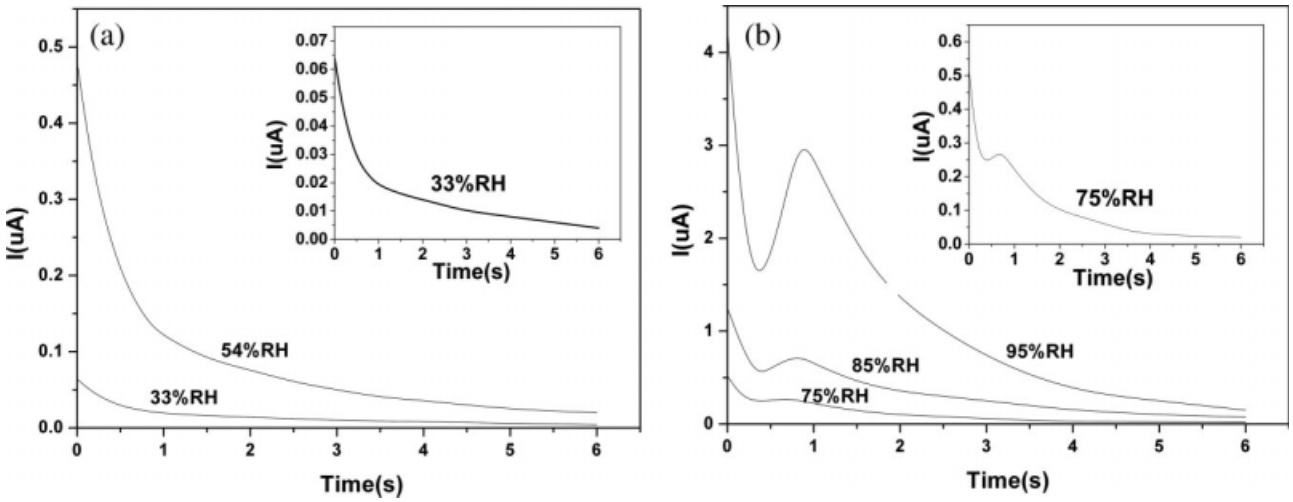

Figure 9 Results of the dc circuit test: (a) low-humidity conditions and (b) high-humidity conditions I, direct current.

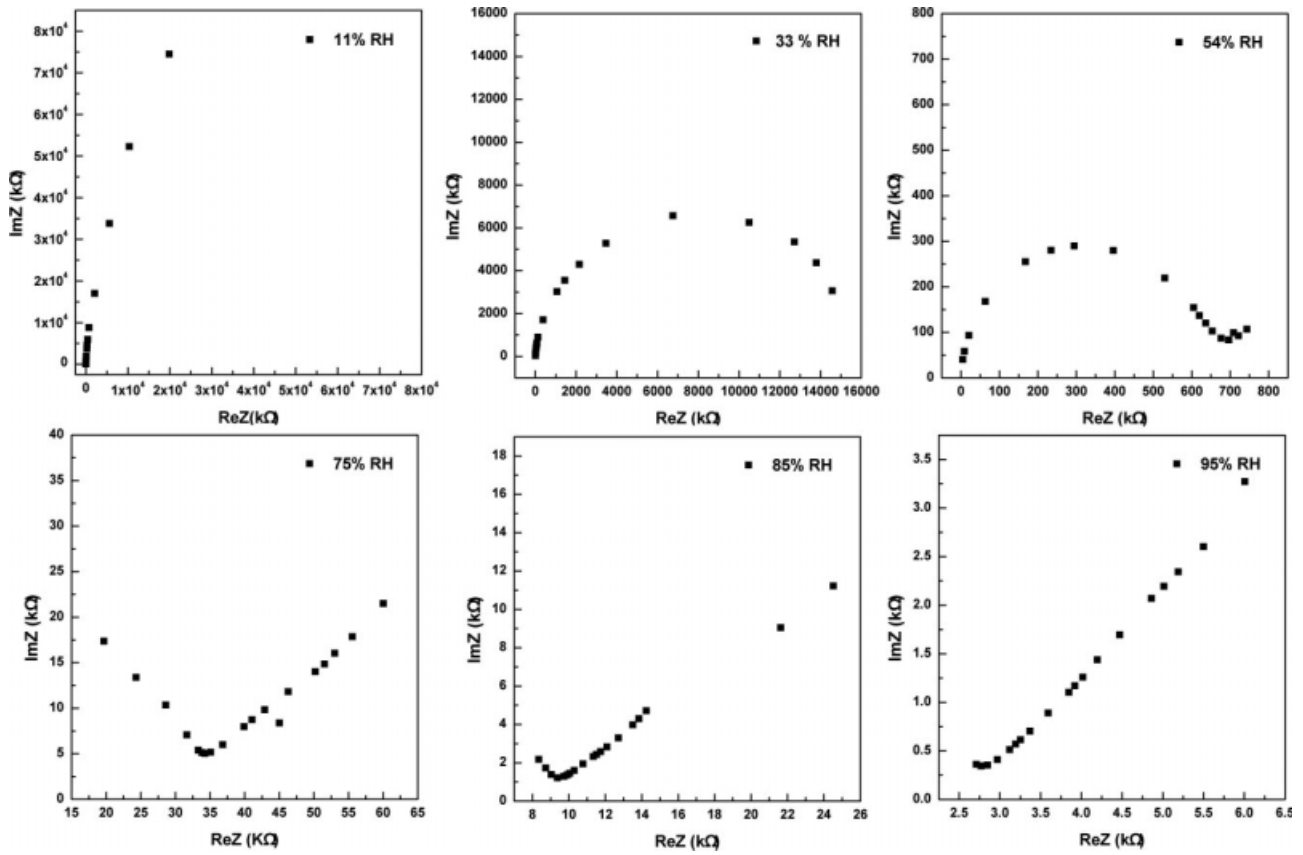

Figure 10 Complex impedance plots of the humidity sensor measured in the indicated humidity environments. ImZ, imaginary part; ReZ, real part.

no significant change in the impedance during this period.

Sensitive mechanism

First, we investigated the humidity sensor by dc analysis. To identify the conducting carriers, a dc circuit of instantaneous polarity reversion was designed by our group. The operation principle was that when the humidity sensor stabilized in one of the humidity environments, the direction of the electrical current was changed. Because the different carriers had different transmitting speeds, the current variation embodied the conducting carrier change. The operation voltage was 1 V, and the current variations at different humidity ranges are shown in Figure 9.

In low-humidity environments, the current decreased linearly with increasing time [Fig. 9(a)]. This indicated that only one type of carrier dominated the conduction in low-humidity environments. We concluded that this carrier was the electron. When the humidity became high, another peak was obtained on the curve. [Fig. 9(b)] The peak became higher when the humidity increased. This phenomenon indicated that another kind of carrier took part in conduction and its function strengthened with increasing humidity. Because this kind of carrier's transmission speed was slower than the electron's transmission speed, another peak was obtained on the current curve. We concluded that the principal conductive particle in high humidity was the ion. The transmission speed of the ion was lower than that of the electron.

We used an ac test method to investigate the humidity sensor. Figure 10 displays the typical complex impedance spectra under different RH conditions. We selected 20 Hz as the initial operation frequency, and the operation frequency was increased 1 by 1 until it reached 100 Hz. There were as many as 20 frequency points that we selected between 20 and 100 Hz. At very low humidity, only part of a semicircle was observed in the plot (11% RH); with increasing RH, an intact semicircle was observed. A straight line was observed in the low-frequency part (33–54% RH). Up to this stage, the vapor pressure was still low, so that the intrinsic electrons were the main contributors to the conduction. When the humidity reached a higher value, the semicircle at high frequency disappears, and only the straight line was left at low frequency (75–95% RH). This straight line was considered to be mainly due to the ion conduction. As the humidity increased, the principal conductive carriers also

changed. Although the ac and dc testing methods differed, we found that both of them showed the same result: electron and then ion conduction dominated as the humidity increased. So the sensitivity mechanism was established through the dc and ac investigation.

CONCLUSIONS

A humidity sensor made by the encapsulation of NiO-doped PPy into mesoporous silica SBA-15, and the humidity-sensing properties were tested. The results show that the encapsulation of NiO-doped PPy into mesoporous silica SBA-15 modified its humidity-sensing properties. We used dc and ac testing to study the sensitivity properties of the sensor and concluded that the conductive particles were different at different humidities.

References

1. Li, Y.; Yang, M. J.; She, Y. Talanta 2004, 62, 707.
2. Parvatikar, N.; Jain, S.; Khasim, S.; Revansiddappa, M.; Bhoraskar, S. V.; Ambika Prasad, M. V. N. Sens Actuators B 2006, 114, 599.
3. Chen, H. W.; Wu, R. J.; Chan, K. H.; Sun, Y. L.; Su, P. G. Sens Actuators B 2005, 104, 80.
4. Feng, C. D.; Sun, S. L.; Wang, H.; Segre, C. U.; Stetter, J. R. Sens Actuators B 1997, 40, 217.
5. Kim, J. W.; Liu, F.; Choi, H. J.; Hong, S. H.; Joo, J. Polymer 2003, 44, 289.
6. Cho, J. H.; Yu, J. B.; Kim, J. S.; Sohn, S. O.; Lee, D. D.; Huh, J. S. Sens Actuators B 2005, 108, 389.
7. Tandon, R. P.; Tripathy, M. R.; Arora, A. K.; Hotchandani, S. Sens Actuators B 2006, 114, 768.
8. Pokhrel, S.; Nagaraja, K. S. Sens Actuators B 2003, 92, 144.
9. Sundaram, R.; Nagaraja, K. S. Phys Status Solidi A 2004, 201, 529.
10. Zhang, Y. S.; Yu, K.; Jing, D. S.; Zhu, Z. Q.; Geng, H. R.; Luo, L. Q. Appl Surf Sci 2005, 242, 212.
11. Dai, C. L.; Liu, M. C.; Chen, F. S.; Wu, C. C.; Chang, M. W. Sens Actuators B 2007, 123, 896.
12. Jain, M. K.; Bhatnagar, M. C.; Sharma, G. L. Sens Actuators B 1999, 55, 180.
13. Tai, W. P.; Oh, J. H. Sens Actuators B 2002, 85, 154.
14. Makhlouf, S. A.; Khalil, K. M. S. Solid State Ionics 2003, 164, 97.
15. Geng, W. C.; Wang, R.; Li, X. T.; Zou, Y.; Zhang, T.; Tu, J. T.; He, Y.; Li, N. Sens Actuators B 2007, 127, 323.
16. Zhang, T.; Wang, R.; Geng, W. C.; Li, X. T.; Qi, Q.; He, Y.; Wang, S. J. Sens Actuators B 2008, 128, 482.
17. Su, P. G.; Sun, Y. L.; Wang, C. S.; Lin, C. C. Sens Actuators B 2006, 119, 483.
18. Wang, C. T.; Wu, C. L. Thin Solid Films 2006, 496, 658.
19. Zhang, W. X.; Wen, X. G.; Yang, S. H. Langmuir 2003, 19, 4420.
20. Qu, L. T.; Shi, G. Q.; Chen, F. E.; Zhang, J. X. Macromolecules 2003, 36, 1063.
21. Geng, W. C.; Li, X. L.; Li, N.; Zhang, T.; Wang, W.; Qiu, S. L. J Appl Surf Sci 2006, 102, 3301.
22. Agarwal, S.; Sharma, G. L. Sens Actuators B 2002, 85, 205.